

## The emergence of braided magnetic fields

C. Prior & D. MacTaggart

To cite this article: C. Prior & D. MacTaggart (2016): The emergence of braided magnetic fields, Geophysical & Astrophysical Fluid Dynamics, DOI: [10.1080/03091929.2016.1216552](https://doi.org/10.1080/03091929.2016.1216552)

To link to this article: <http://dx.doi.org/10.1080/03091929.2016.1216552>



Published online: 29 Jul 2016.



Submit your article to this journal [↗](#)



View related articles [↗](#)



View Crossmark data [↗](#)



# The emergence of braided magnetic fields

C. Prior<sup>a</sup> and D. MacTaggart<sup>b</sup>

<sup>a</sup>Department of Mathematical Sciences, Durham University, Durham, UK; <sup>b</sup>School of Mathematics and Statistics, University of Glasgow, Glasgow, UK

## ABSTRACT

We study the emergence of braided magnetic fields from the top of the solar interior through to the corona. It is widely believed that emerging regions smaller than active regions are formed in the upper convection zone near the photosphere. Here, bundles of braided, rather than twisted, magnetic field can be formed, which then rise upward to emerge into the atmosphere. To test this theory, we investigate the behaviour of braided magnetic fields as they emerge into the solar atmosphere. We compare and contrast our models to previous studies of twisted flux tube emergence and discuss results that can be tested observationally. Although this is just an initial study, our results suggest that the underlying magnetic field structure of small emerging regions need not be twisted and that braided field, formed in the convection zone, could suffice.

## ARTICLE HISTORY

Received 28 April 2016

Accepted 20 July 2016

## KEYWORDS

Magnetohydrodynamics;  
Magnetic flux emergence;  
Braids

## 1. Introduction

The Sun's toroidal magnetic field is revealed by the presence of emerging flux at its surface, the photosphere. Concentrations of magnetic field that appear at the photosphere can vary in complexity but are generally bipolar, with two fairly distinct areas of opposite polarity (Schrijver and Zwaan 2000). This pattern appears across a range of scales, from the 'salt and pepper' fields of the quiet Sun (e.g. Meyer *et al.* 2013) to full active regions that can be hundreds of megametres in length. Despite a certain amount of self-similarity across the length scales, including the eruptive capabilities of smaller ephemeral regions (Schrijver 2010), it is generally believed that the processes which create large active regions are different to those of smaller regions. For smaller regions, it is widely accepted that magnetic field in the turbulent convection zone near the photosphere is deformed into 'tangled bundles' which can rise and emerge into the atmosphere (e.g. Stein *et al.* 2011, Stein 2012). For larger regions, there remains some debate as to whether the magnetic fields form at the base of the convection zone or within it (e.g. Fan 2001, Barker *et al.* 2012).

As mentioned above, emerging regions take the form of 'tangled bundles' of magnetic field. In modelling, it is generally assumed that such bundles of magnetic field are twisted flux tubes. This is because, without twist, flux tubes break up into magnetic vortices (in a similar way to a Von Kármán vortex street) and lose their structure (e.g. Emonet and Moreno-Insertis 1998, Fan *et al.* 1998). However, even with twist, flux tubes can suffer

substantial deformation in the highly turbulent convection zone near the photosphere (e.g. [Bushby and Archontis 2012](#)) unless their magnetic pressure is strong enough to dominate the pressure of the plasma outwith the flux tube, i.e. that of the surrounding convection zone. Although achieving strong field strengths may be possible for large active regions, this is less certain for smaller regions. Magnetoconvection models ([Stein 2012](#)) have shown that tangled bundles of magnetic field can form close to the photosphere. These bundles are not necessarily twisted and suggest that twisted flux tubes may not be the best model for smaller regions. In this paper, we investigate the emergence of braided, as opposed to twisted, magnetic fields. Such fields could be created in the convection zone as suggested by simulations (e.g. [Stein and Nordlund 2012](#)). Note that, by braided, we mean entangled in a manner more complex than simple twisting, rather than any precise mathematical definition. The emergence behaviour of such regions in the solar atmosphere has not been previously investigated. If their behaviour in the atmosphere, once they have emerged, is consistent with observations, this could imply that the property of twist in the underlying magnetic fields is not particularly important for smaller regions.

The paper is outlined as follows. First, we will describe the model, including the main equations and an account of how to construct braided magnetic fields. This is followed by a description of the diagnostic tools that we use to analyze the simulations and the analysis itself. The paper concludes with a discussion of possible observational signatures from the model and some general conclusions.

## 2. Model setup

### 2.1. Theoretical framework

In this study, we shall consider small active regions of  $O(10)$  Mm across. This ties in with the theoretical considerations discussed in the Introduction and allows us to make comparisons with twisted flux tube models that are of a similar size ([Hood \*et al.\* 2012](#), [Cheung and Isobe 2014](#)). As our focus is on the dynamics of the magnetic field, we shall consider an idealized description of the solar atmosphere. The bulk properties of the plasma and magnetic field dynamics are described by compressible magnetohydrodynamics (MHD). The 3D resistive and compressible MHD equations are solved using a Lagrangian remap scheme ([Arber \*et al.\* 2001](#)). In dimensionless form, the MHD equations are

$$\frac{D\rho}{Dt} = -\rho \nabla \cdot \mathbf{u}, \quad (1)$$

$$\frac{D\mathbf{u}}{Dt} = -\frac{1}{\rho} \nabla p + \frac{1}{\rho} (\nabla \times \mathbf{B}) \times \mathbf{B} + \frac{1}{\rho} \nabla \cdot \boldsymbol{\sigma} + \mathbf{g}, \quad (2)$$

$$\frac{D\mathbf{B}}{Dt} = (\mathbf{B} \cdot \nabla) \mathbf{u} - (\nabla \cdot \mathbf{u}) \mathbf{B} + \eta \nabla^2 \mathbf{B}, \quad (3)$$

$$\frac{D\varepsilon}{Dt} = -\frac{p}{\rho} \nabla \cdot \mathbf{u} + \frac{1}{\rho} \eta |\mathbf{j}|^2 + \frac{1}{\rho} Q_{\text{visc}}, \quad (4)$$

$$\nabla \cdot \mathbf{B} = 0, \quad (5)$$

with specific energy density

$$\varepsilon = \frac{P}{(\gamma - 1)\rho}. \quad (6)$$

The basic variables are the density  $\rho$ , the pressure  $p$ , the magnetic induction  $\mathbf{B}$  (referred to as the magnetic field) and the velocity  $\mathbf{u}$ .  $\mathbf{j}$  is the current density,  $\mathbf{g}$  is gravity (uniform in the  $z$ -direction) and  $\gamma = 5/3$  is the ratio of specific heats. The dimensionless temperature  $T$  can be found from

$$T = (\gamma - 1)\varepsilon. \quad (7)$$

We make the variables dimensionless against photospheric values, namely pressure  $p_{\text{ph}} = 1.4 \times 10^4$  Pa; density  $\rho_{\text{ph}} = 2 \times 10^{-4}$  kg m $^{-3}$ ; scale height  $H_{\text{ph}} = 170$  km; surface gravity  $g_{\text{ph}} = 2.7 \times 10^2$  m s $^{-2}$ ; speed  $u_{\text{ph}} = 6.8$  km s $^{-1}$ ; time  $t_{\text{ph}} = 25$  s; magnetic field strength  $B_{\text{ph}} = 1.3 \times 10^3$  G and temperature  $T_{\text{ph}} = 5.6 \times 10^3$  K. In the non-dimensionalization of the temperature we use a gas constant  $\mathcal{R} = 8.3 \times 10^3$  m $^2$  s $^{-2}$  K $^{-1}$  and a mean molecular weight  $\tilde{\mu} = 1$ .  $\eta$  is the resistivity and we take its value to be  $10^{-3}$ . This value is close to the lowest physical resistivity that can be chosen before numerical resistivity dominates (see [Arber et al. 2007](#), [Leake et al. 2013](#)). The fluid viscosity tensor and the viscous contribution to the energy equation are respectively

$$\boldsymbol{\sigma} = 2\mu \left[ \mathbf{D} - \frac{1}{3}(\text{tr} \mathbf{D})\mathbf{I} \right] \quad (8)$$

and

$$Q_{\text{visc}} = \boldsymbol{\sigma} : \nabla \mathbf{u}, \quad (9)$$

where

$$\mathbf{D} = \frac{1}{2} \left( \nabla \mathbf{u} + \nabla \mathbf{u}^T \right) \quad (10)$$

is the symmetric part of the rate of strain tensor and  $\mathbf{I}$  is the identity tensor. We take  $\mu = 10^{-5}$  and use this form of viscosity primarily to aid stability. The code accurately resolves shocks by using a combination of shock viscosity ([Wilkins 1980](#)) and Van Leer flux limiters ([van Leer 1979](#)), which add heating terms to the energy equation. Values will be expressed in non-dimensional form unless explicitly stated otherwise.

The equations are solved in a Cartesian computational box of (non-dimensional) sizes  $[-45, 45] \times [-45, 45] \times [0, 135]$  in the  $x$ ,  $y$  and  $z$  directions respectively. The boundary conditions are closed on the top and base of the box and periodic on the sides. Damping layers are included at the side and top boundaries to reduce the reflection/transmission of waves. The computational mesh contains  $288 \times 288 \times 432$  points.

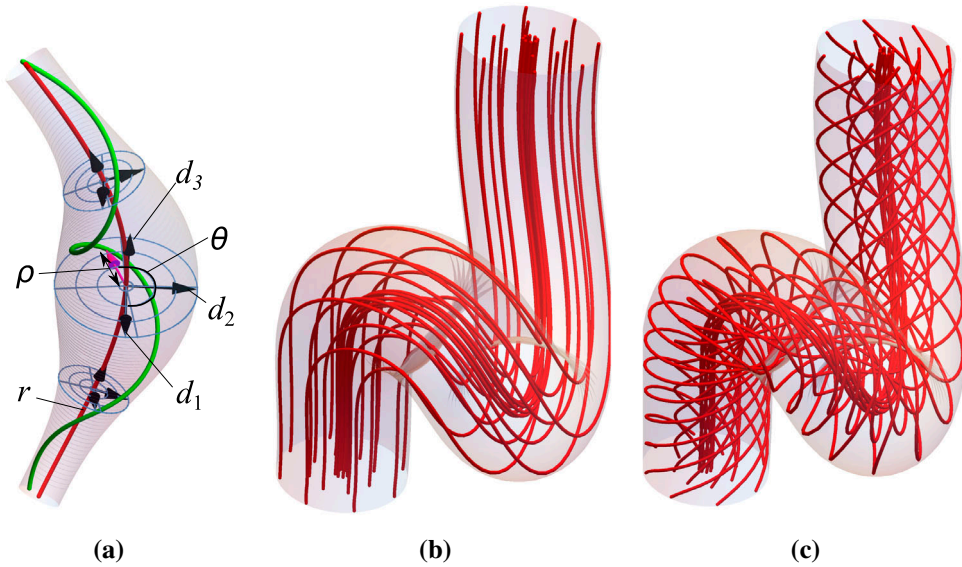


**Figure 1.** Illustrations of the curvilinear geometry used in this study. Panel (a) depicts the curvilinear coordinate system  $T(s, \rho, \theta)$ ; also shown in green is an example curve as well as the orthonormal basis  $(d_1, d_2, d_3)$ . Panel (b) depicts a domain  $T$  filled with field lines created by parallel transport, while (c) depicts a domain  $T$  filled with twisted field lines.

## 2.2. Initial background atmosphere

The idealized initial equilibrium atmosphere is given by prescribing the temperature profile

$$T(z) = \begin{cases} 1 - [(\gamma - 1)/\gamma]z, & z < z_{\text{ph}}, \\ 1, & z_{\text{ph}} \leq z \leq z_{\text{tr}}, \\ T_{\text{cor}}^{[(z-z_{\text{tr}})/(z_{\text{tr}}-z_{\text{ph}})]}, & z_{\text{tr}} < z < z_{\text{cor}}, \\ T_{\text{cor}}, & z \geq z_{\text{cor}}, \end{cases} \quad (11)$$

where  $T_{\text{cor}} = 150$  is the initial coronal temperature,  $z_{\text{ph}}$  is the base of the photosphere,  $z_{\text{tr}} = z_{\text{ph}} + 10$  is transition and  $z_{\text{cor}} = z_{\text{ph}} + 20$  is the base of the corona. In this paper,  $z_{\text{ph}} = 30$ . The solar interior is defined by  $z < z_{\text{ph}}$  and is convectively stable in order to focus on the dynamics of the emerging magnetic braid. The other state variables, pressure and density, are found by solving the hydrostatic equation in conjunction with the ideal equation of state

$$\frac{dp}{dz} = -\rho g, \quad p = \rho T. \quad (12a,b)$$

For simplicity and since this is the first study of emerging magnetic braids, we assume that there is no ambient magnetic field. This choice also helps us to facilitate comparisons with other flux emergence models (e.g. Murray *et al.* 2006, Fan 2008, Hood *et al.* 2009, MacTaggart and Hood 2009b). To study emergence, we must place a particular form for the magnetic field in the solar interior and apply a perturbation to allow it to emerge. Before presenting the models that we will consider in this study, we now briefly review

the technique for creating magnetic flux tubes with arbitrary axial geometry introduced in [Prior and Yeates \(2016a\)](#).

### 2.3. Creating the flux tubes

We consider flux tubes embedded in a Cartesian coordinate system  $(x, y, z)$ . The ultimate aim is to define a tube (of possibly varying radius) whose interior is filled with a specified set of curves; that is to say, we specify its precise topology. A divergence-free field  $\mathbf{B}$  whose field lines have this exact topology is then created.

The tube's axis is specified by a curve  $\mathbf{r}(s) : [0, L] \rightarrow \mathbb{R}^3$ . A right-handed moving orthonormal basis  $(\mathbf{d}_1, \mathbf{d}_2, \mathbf{d}_3)$  is defined for  $\mathbf{r}$  with  $\mathbf{d}_3 = \mathbf{r}'(s)/|\mathbf{r}'(s)|$  being the unit tangent vector of  $\mathbf{d}_3$ ,  $\mathbf{d}_1$  a vector field always normal to  $\mathbf{d}_3$  ( $\mathbf{d}_1 \cdot \mathbf{d}_3 = 0$ ) and  $\mathbf{d}_2 = \mathbf{d}_3 \times \mathbf{d}_1$ . The use of such moving frames is standard in thin rod and polymer elasticity ([Antman 2005](#)). This basis can then be extended to form a curvilinear coordinate system by defining a map  $T(s, \rho, \theta) : [0, L] \times [0, 1] \times \mathbb{S}^1 \rightarrow \mathbb{R}^3$  as

$$T(s, \rho, \theta) = \mathbf{r}(s) + \rho(s)R(s)\{\mathbf{d}_1(s) \cos[\theta(s)] + \mathbf{d}_2(s) \sin[\theta(s)]\}. \quad (13)$$

This coordinate system is shown in figure 1(a). The evolution of this basis with  $s$ , the arclength of  $\mathbf{r}(s)$ , is determined by the linear ODEs

$$\begin{pmatrix} \mathbf{d}'_1 \\ \mathbf{d}'_2 \\ \mathbf{d}'_3 \end{pmatrix} = \begin{pmatrix} 0 & 0 & -u_2 \\ 0 & 0 & u_1 \\ u_2 & -u_1 & 0 \end{pmatrix} \begin{pmatrix} \mathbf{d}_1 \\ \mathbf{d}_2 \\ \mathbf{d}_3 \end{pmatrix}, \quad (14)$$

where  $u_1$  and  $u_2$  are functions determining the curvature of  $\mathbf{r}_1$  about the two orthogonal directions  $\mathbf{d}_1$  and  $\mathbf{d}_2$ . Readers familiar with the differential geometry of tubes will recognise that in this choice of basis the vector field  $\mathbf{d}_1$  is parallel-transported along  $\mathbf{r}$  ([Bishop 1975](#)). This means that the curves of fixed coordinates  $R = \text{const.}$  and  $\theta = \text{const.}$  will follow the shape of the tube (figure 1(b)), i.e. it is the simplest possible topology given the tube's shape. We can then impart more complex topology on the tube by specifying functions  $\rho(s)$  and  $\theta(s)$  for each curve of the field, a simple example being  $\rho(s) = \text{const.}$  and  $\theta(s) = 2\pi s T_w/L$  for all curves, which will generate a twisted tube with total twist  $T_w$  (figure 1(c)).

### 2.4. Generating the magnetic field

A set of curves determined by the functions  $\rho(s)$  and  $\theta(s)$  and the map (13) determine a unit tangent field  $\mathbf{N}$  at all points in the domain  $T$ . We turn this field into a divergence-free field  $\mathbf{B}$  by writing  $\mathbf{B} = \phi \mathbf{N}$  and solving the PDE

$$\nabla \cdot \mathbf{B} = \nabla \phi \cdot \mathbf{N} + \phi \nabla \cdot \mathbf{N} = 0, \quad (15)$$

whose solution via the method of characteristics (integrating along field lines  $f(s)$ ) is

$$\mathbf{B}(f(s)) = N \phi_0 \exp\left(-\int_0^s \nabla \cdot \mathbf{N} \, dl\right), \quad (16)$$

where  $\phi_0$  is the distribution of  $\phi$  on the surface  $s = 0$ . So, in order to define the flux tube magnetic field we have to specify

- (i) The internal topology, through functions  $\rho(s)$  and  $\theta(s)$  determining the paths of curves in the domain.
- (ii) The magnetic flux distribution  $\phi_0$  on one end of the tube.

We then integrate (16) to determine the full field. A further embellishment of this process is to select a finite number of curves  $\mathbf{r}_i$  from the original tube  $T$  and to create smaller tubular fields surrounding each curve  $\mathbf{r}_i$ . In this way, a pigtail braided field with a sigmoidal axis was created in [Prior and Yeates \(2016a\)](#) (an example is shown later in figure 3). A second approach to increasing the complexity of the field is to define fields which partly overlap, creating a composite field with more complex internal topology. This is used in what follows to develop a version of the braided field used in [Yeates \*et al.\* \(2010\)](#), [Wilmot-Smith \*et al.\* \(2011\)](#), [Yeates \*et al.\* \(2015\)](#). The technical details of the process by which this field is interpolated onto a Cartesian grid are discussed in [Prior and Yeates \(2016a\)](#).

## 2.5. Braid models

Now that we have described how to form flux tubes, we will now present the fields of interest to this study. In what follows we choose the axis curve  $\mathbf{r}$  to be a half circle with radius  $R_m$ , i.e.

$$\mathbf{r}(s) = [R_m \cos(s/R_m), 0, R_m \sin(s/R_m)], \quad (17)$$

where  $s \in [0, \pi R_m]$ .

### 2.5.1. Uniform twist

As mentioned above, the choices  $R = \text{const.}$  (constant tube width) and  $\theta(s) = 2\pi s T_w / L$  define a field with uniform twist and a total rotation of  $2\pi T_w$  radians. We constructed fields with  $T_w = 2$  and  $T_w = 5$ . These values are below and above, respectively, the kink instability threshold for toroidal magnetic flux ropes (e.g. [Török and Kliem 2005](#)). The major radius is  $R_m = 17.5$  and the tube radius  $R = 3.75$ . These magnetic fields were used for test runs to make sure that their emergence properties behaved in accordance with other twisted flux tube models (e.g. [Hood \*et al.\* 2009](#), [MacTaggart and Hood 2009a,b](#)). We will not discuss the emergence of these twisted fields, which has been treated at length in existing literature, and instead focus entirely on the braided fields described below.

### 2.5.2. B4 braid

This field is based on the numerical experiments of [Wilmot-Smith \*et al.\* \(2009, 2011\)](#) and [Russell \*et al.\* \(2015\)](#), where a family of braided magnetic fields were created using series of  $n$  opposing pairs of rotations through an angle  $\pi$  rad at staggered distances along the tube's length. In this case we use four pairs of opposing twist (hence B(braided)4). We impose this twisted structure on a half circle of major radius  $R_m = 17.5$ . We then define two curves  $\mathbf{r}_i, i = 1, 2$  as

$$\mathbf{r}_i = \mathbf{r} + \rho^i \mathbf{n} \cos(\theta_i), \quad \theta_i = 0, \pi. \quad (18)$$

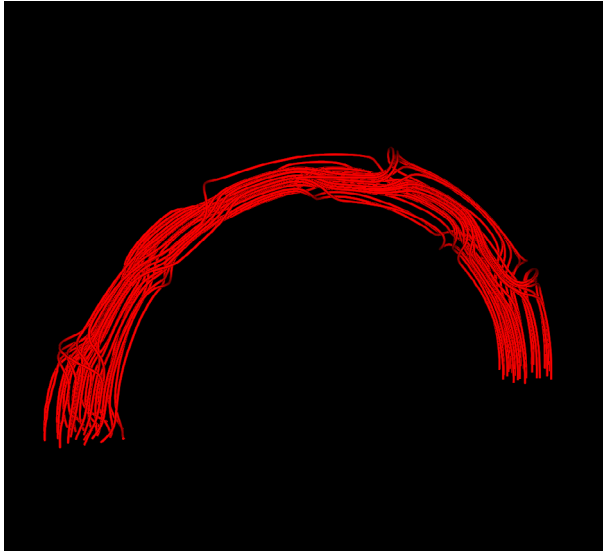


**Figure 2.** Sample field lines of the  $B_4$  field depicting its internal complexity.

These curves are then used to define two tubes  $T_i$ ,  $i \in 1, 2$ . The values of  $\rho^i = 0.15$  and the tube radii  $R_i = 2.8$  are chosen so that the tubes have significant overlap (increasing the field's complexity). We then define the fields within the tubes with the following topology functions:

$$\rho_{1/2} = \text{const.}, \quad (19a)$$

$$\theta_1(s) = \sum_{k=1}^4 \frac{\pi}{1 - \exp(-a(s - b_{1k}))}, \quad \theta_2(s) = \sum_{k=1}^4 \frac{\sigma\pi}{1 - \exp(-a(s - b_{2k}))}, \quad (19b,c)$$

with  $\sigma = -1$  and  $b_{11} < b_{21} < b_{12} < b_{22} < b_{13} < b_{23} < b_{14} < b_{24}$ . This creates a series of staggered twists of the field, with the twist occurring sequentially in tube  $T_1$  then  $T_2$  then  $T_1$  again, etc. The choice  $\sigma = -1$  means that the rotations have opposing chirality. In practice the values of  $b_{1i}, b_{2i}$  and  $a$  are chosen so that there is no overlap (when one tube has twisted field lines, the field lines of tube 2 are created by parallel transport). These two prescriptions of  $\theta_{1/2}$  can be used to make fields  $\mathbf{B}_1$  and  $\mathbf{B}_2$ ; the  $B_4$  field is their sum  $\mathbf{B}_{B_4} = \mathbf{B}_1 + \mathbf{B}_2$ . Field lines of this composite field are shown in figure 2. It is difficult to see in this curved geometry but sets of the field lines can be shown to form pigtail braids (Wilmot-Smith *et al.* 2011). For this model, the average field strength at  $t = 0$  is  $B \sim 20$ . This value results in an initial average plasma beta for the tube of  $\beta = 2p/B^2 \sim 10$ . This means that the field is dynamically dominated by the flow in the solar interior. The initially high value of  $B$  is chosen to ensure sensible values (i.e. those in line with twisted tube models) of the field strength when the tube reaches the photosphere and emerges into the atmosphere. Since we are not modelling convection, the model solar interior acts like an extended boundary condition, allowing flux emergence at the photosphere to occur without imposing any motions there. The average magnetic field strength in the model solar interior decays in time and by  $t = 40$  it is about 10% of its value at  $t = 0$ .

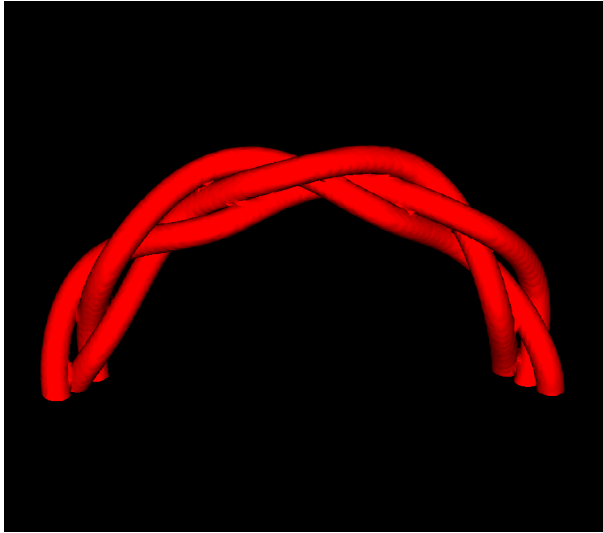


**Figure 3.** Current contours of the pigtail field used in this study. Current contours rather than field lines are shown for clarity.

In [Wilmot-Smith \*et al.\* \(2011\)](#) it was found that the diffuse small scale current structure of this braid leads to rapid and efficient reconnection, causing the field to separate into two twisted flux ropes of opposing chirality. These results were recreated using flux ropes with realistic coronal morphology in [Prior and Yeates \(2016b\)](#). Since the Alfvén travel time in our model solar interior is much longer than the typical coronal value, we will pay close attention to whether the entanglement survives the emergence process.

### 2.5.3. Pigtail braid

The pigtail braid, shown in figure 3, is made up of three flux ropes  $r_i$  which interlink within a toroidal tube  $T$  of major radius  $R_m = 17.5$ . The axes of the three sub-tubes are defined by the functions

$$\begin{aligned} \rho_i(s) &= 0.5\sqrt{\sin(2\pi s/L + d_i)^2 + \cos(4\pi s/L + d_i)^2}, \\ \theta_i(s) &= \arctan\left[\frac{\cos(4\pi s/L + d_i)}{\sin(2\pi s/L + d_i)}\right], \end{aligned} \quad \begin{cases} d_1 = 0, \\ d_2 = 1/3, \\ d_3 = 2/3. \end{cases}$$

We then create tubular fields  $\mathbf{B}_i$  in tubes  $T_i$  of fixed radius  $R = 1.2$  around each of these axes. In this study, for simplicity, we choose the fields to have no internal twisting. The average field strength at  $t = 0$  is  $B \sim 10$ . The plasma beta then has the value  $\beta \sim 20$ . This means that in the solar interior, as for the B4 braid, the magnetic field is dominated dynamically by flows. In contrast to the B4 braid, however, the only significant current structure will be between the tubes rather than in the interior. In [Prior and Yeates \(2016b\)](#) it was found that this meant the disentanglement of the field through reconnection is far less efficient. Once again we will pay attention to how well the pigtail structure survives the emergence process in what follows.

## 2.6. Perturbing the braids

The models described above are placed in the solar interior ( $z_{\text{ph}} < 0$ ). In order to cause these tubes to rise towards the photosphere and emerge into the atmosphere, some perturbation of the field must be induced. This perturbation normally takes the form of introducing a density deficit into the tube (MacTaggart and Hood 2009a,b, Hood *et al.* 2012, MacTaggart *et al.* 2015) or the application of a small velocity perturbation (e.g. Magara and Longcope 2001, Magara and Longcope 2003, An and Magara 2013). In this study we opt for the latter and apply a perturbation to the velocity, at the initial tube position, of the form

$$v_p = V_0 \exp\left(-\frac{x^2}{x_0^2}\right) \exp\left(-\frac{y^2}{y_0^2}\right) \exp\left(-\frac{(z - R_m)^2}{z_0^2}\right) \sin\left(\frac{t}{t_0}\pi\right).$$

After some experimentation, we chose the parameter values  $V_0 = 0.05$ ,  $x_0 = 5$ ,  $y_0 = 3$ ,  $z_0 = 5$  and  $t_0 = 6$ . The effect of using these parameters results in a field evolution in the model solar interior similar to that described in Hood *et al.* (2012). If the parameters are too large, the entire tube is dragged up into the atmosphere, producing unrealistic results. With the chosen set of parameters, the field rises to the photosphere in a similar time scale to other studies. At the photosphere, the majority of the magnetic flux becomes trapped and cannot rise via buoyancy, due to the change in temperature gradient. To push into the atmosphere, the magnetic field strength must build up until the magnetic pressure can defeat the plasma pressure, and a buoyancy instability occurs. As the initial onset of emergence in this study is very similar to that described extensively in other works, we shall focus on the emergence behaviour as the field pushes into the atmosphere.

## 3. Simulations

Even in idealized models, such as those presented in this paper, the coronal magnetic fields that develop from flux emergence can become very complicated. Before presenting the results of our simulations we describe some the diagnostic tools that we use to study the magnetic fields.

### 3.1. Diagnostics

#### 3.1.1. Current contours

We plot contours of constant current magnitude  $\|j\|$  in order to track the field's expansion through the photosphere, transition region and the corona. For the majority of plots we choose a value of  $\|j\| = 0.1$  in the interior/photosphere and a lower value  $\|j\| = 0.001$  when the field is in the transition region/corona. Both values are chosen in order to reliably observe the key features of the current distribution. For similar plots that do not use the above values, appropriate details will be given in captions.

#### 3.1.2. Current and density slices in the corona

As the magnetic field expands into the corona, dense plasma can be carried upwards from the photosphere. If this field expands so that it becomes too weak to support the dense photospheric plasma, the field lines can buckle and dips containing dense plasma can form. This is effectively the magnetic Rayleigh Taylor instability, where the dense overlying

plasma can no longer be supported and begins to sink. This process continues until the magnetic tension of the dipped field ( $\mu_0^{-1} \mathbf{B} \cdot \nabla \mathbf{B}$ ) can balance the gravitational force of the collected dense plasma. In order to find these dipped locations in our models, where magnetic geometries are highly complex, a simple and effective method is to compare slices of the current density magnitude  $\|\mathbf{j}\|$  and density  $\rho$  distributions across the same  $z$ -planes.

### 3.1.3. Synthetic magnetograms

We create predicted magnetograms by plotting the value of  $B_z$  at the photosphere  $z_{\text{ph}}$ . These maps can be used for qualitative comparisons to observations, i.e. the shape and evolution of the large scale features of  $B_z$ .

### 3.1.4. Local twist distributions

A quantitative measure of the field's internal geometry which we measure is the average local twisting of each field line. For a field line  $f(l)$  of arclength  $L$  whose footprint coordinates are  $(x_f, y_f)$ , we define the integrated quantity

$$L_f(f(l)) = \frac{1}{L} \int_0^L \frac{\mathbf{j} \cdot \mathbf{B}}{\mathbf{B} \cdot \mathbf{B}} dl = \frac{1}{L} \int_0^L \frac{\mathbf{B} \cdot \nabla \times \mathbf{B}}{\mathbf{B} \cdot \mathbf{B}} dl, \quad (20)$$

which represents the mean rotation of the local field lines around  $f(l)$ . For a linear force-free field,  $\mathbf{j} \cdot \mathbf{B} = \alpha \mathbf{B} \cdot \mathbf{B}$  and  $L_f$  is just the linear force-free parameter  $\alpha$ , which would be constant throughout the domain. This quantity was used to evaluate the internal structure of relaxing braided and twisted cylindrical fields in [Wilmot-Smith \*et al.\* \(2011\)](#), [Yeates \*et al.\* \(2015\)](#) and for flux ropes with more realistic coronal geometries in [Prior and Yeates \(2016a,b\)](#). It was found that braided fields, even with significantly reduced Lorentz forces, can often exhibit significantly mixed  $L_f$  distributions (both positive and negative twisting), indicative of field with complex internal structure. In this study we create distributions of  $L_f$  across the photospheric plane  $z_{\text{ph}}$  and the coronal plane  $z_{\text{cor}} = z_{\text{ph}} + 20$ , in order to evaluate what structures from the initial field has risen into both domains. In addition we draw subsets of field lines on specific domains of these  $L_f$  plots to try to give some perspective on the implication of these distributions.

### 3.1.5. Sigmoid analysis

For a bipolar region, the simplest model for its magnetic field is a potential field. In such a field, the field lines do not kink as they travel from one footprint to the other. The simplest step up in complexity for the magnetic field is a linear force-free field. For this case, there is now a non-zero current density and the bipolar region has a sigmoidal geometry. Sigmoids are, therefore, signatures of current (or twist) in a magnetic field. A clear way to visualize sigmoids in simulations is to calculate a proxy of the emission which might be viewed by line-of-sight imaging in extreme-ultraviolet or X-ray wavelengths (e.g. [Archontis \*et al.\* 2009](#), [Hood \*et al.\* 2012](#)). We average  $\|\mathbf{j}\|^2$  (proportional to the ohmic dissipation) along field lines starting at all points in the domain. The averaging is performed on the assumption that thermal conduction along the field lines occurs much faster than the field evolves. We then integrate this quantity vertically, from  $z_{\text{cor}}$ , to mimic the line-of-sight view. This proxy has been used in a number of previous studies (e.g. [Cheung and DeRosa 2012](#), [Prior and Yeates 2016b](#)).

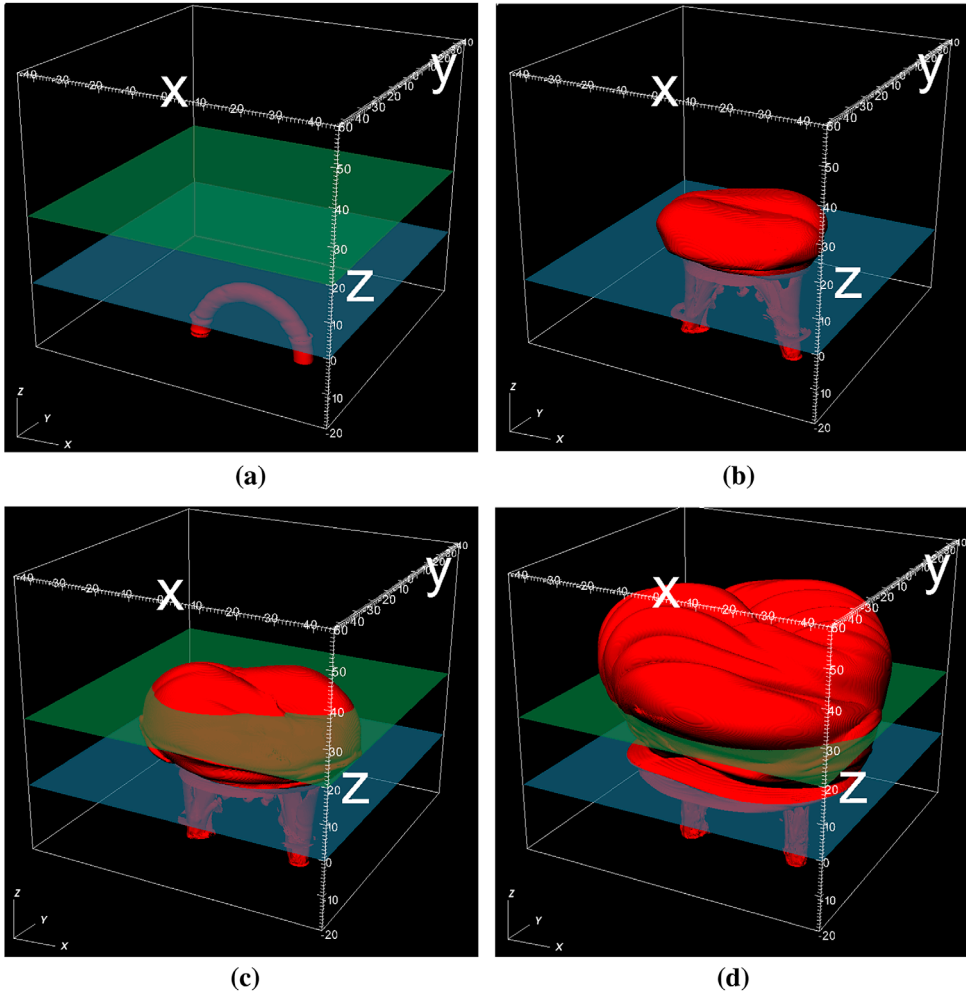


**Figure 4.** Contours of constant current of the B4 field at various times during its evolution. (a)  $t = 0$ , the initial half torus tube is evident. (b)  $t = 20$ , the tube has risen into the photosphere/transition region and expanded with a central dip. (c)  $t = 30$ , further expansion has lead to the emerging field penetrating the corona. (d)  $t = 90$ , a series of undulations have developed in the coronal field. Grey slice:  $z_{\text{ph}}$ , green slice:  $z_{\text{cor}}$ .

### 3.2. B4 field

The field evolves for  $t \in [0, 90]$  during which it expands significantly into the corona. This time scale, for the size of region considered, is comparable to other models using twisted flux tubes (e.g. MacTaggart and Hood 2009b). Exact rise times are dependent on the choice of the initial perturbation and the initial position of the flux tube relative to  $z_{\text{ph}}$ . Figure 4 displays contours of current density at different times in the evolution of the emerging region. The two semi-transparent slices indicate the positions of  $z_{\text{ph}}$  (grey) and  $z_{\text{cor}}$  (green).

Figure 4(a) shows the initial state of the half torus at  $t = 0$ . Later, in figures 4(b)–(d), the effect of a magnetic buoyancy instability causes a large expansion of the field into the atmosphere. In figure 4(d), there is significant penetration into the corona. Much of this

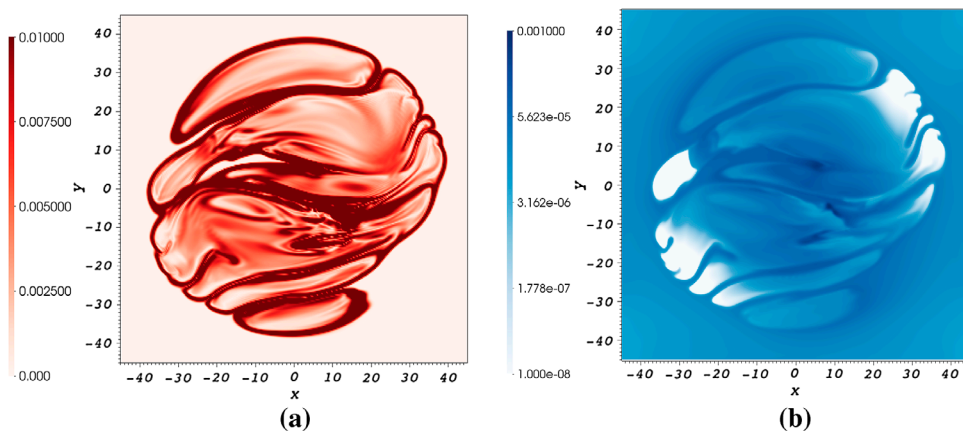
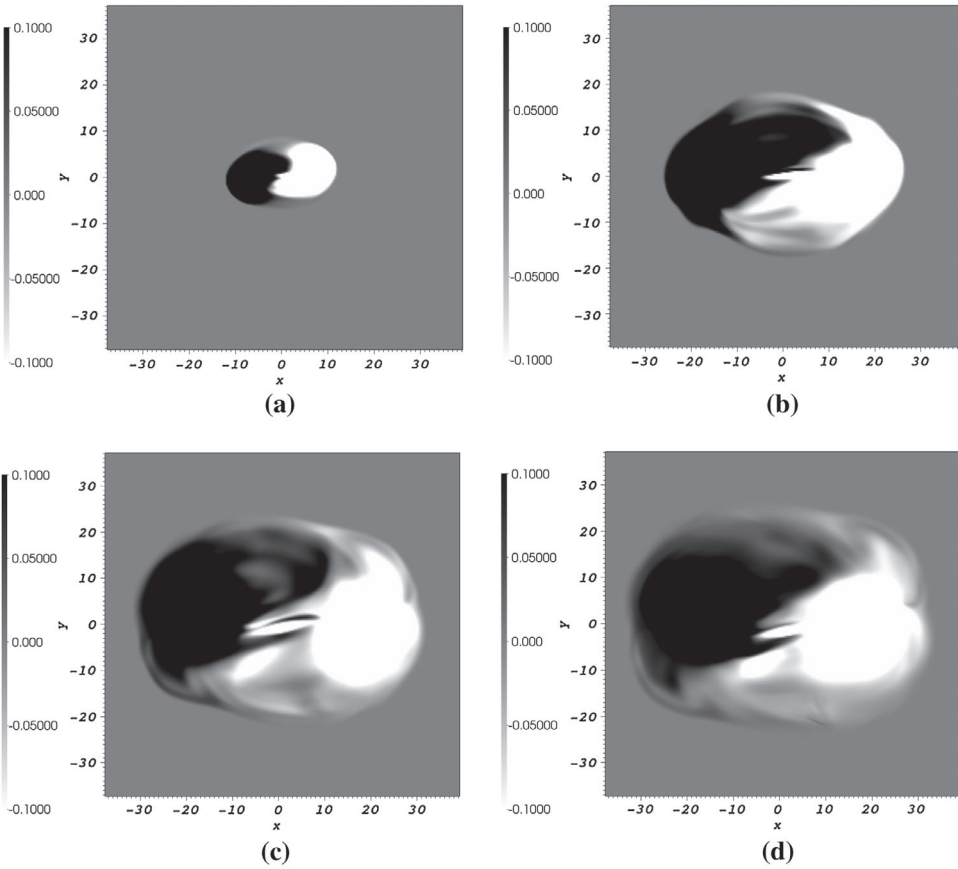


**Figure 5.** Slices of the current magnitude and density distributions at  $z = 87.5$  for  $t = 90$ . (a) the current magnitude (darker colours are higher in magnitude). The ridge structure shown in figure 4(d) is evident. (b) the (logged) density magnitude, the morphology of the distribution matches that of the current distribution in (a).

evolution mirrors what has been found in twisted tube models, including the fact that some magnetic flux remains trapped at the photosphere, shown most clearly in figure 4(d) by the spread of the contour at  $z_{\text{ph}}$  (cf. figure 2 of Hood *et al.* (2012)). The magnetic ‘bubbles’ in figures 4(b)–(d) display distinct undulations. These are caused by the expanding magnetic field bringing up dense plasma which it can no longer fully support. Some of this dense plasma drains back down to the lower atmosphere and some remains trapped in magnetic dips. To show this more clearly, consider the slices displayed in figure 5.

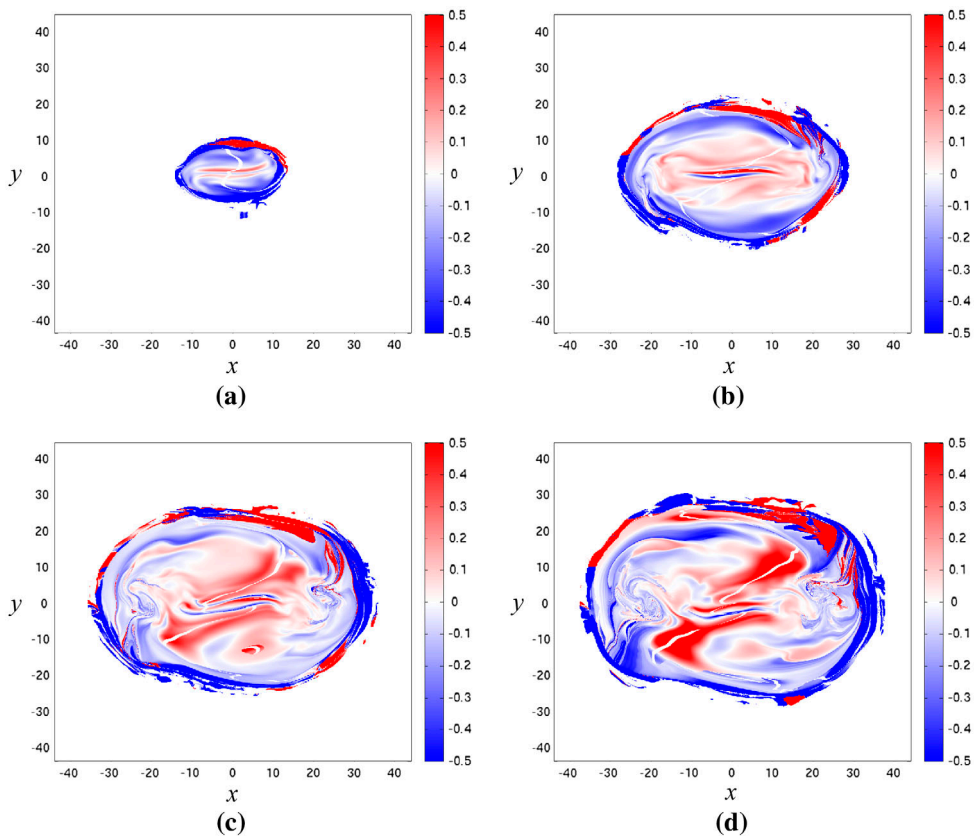
The two slices, taken at  $z = 87.5$  for  $t = 90$ , show (a)  $\|\mathbf{j}\|$  and (b)  $\log \rho$ . What is immediately obvious from these two slices is that morphology of the current density matches that of the (logged) density. This shows that it is presence of dense plasma that is deforming the magnetic field and producing regions of increased current density. The raising of dense plasma occurs also in twisted flux tube models (MacTaggart and Haynes 2014, MacTaggart *et al.* 2015). This process has important implications for what kind of eruptions can take place in emerging solar regions. As this study, however, is an initial foray into the behaviour of braided tube emergence, we shall leave questions related to eruptions and coronal interactions to future work.

Figure 6 displays synthetic magnetograms at four different times throughout the period of emergence. The classic bipolar configuration, described in the Introduction, grows in time. Although the magnetic field expands, the centres of the two main polarities move apart until they are approximately  $2R_m$  apart (the diameter of the half torus anchored at the base of the computational domain). The magnetograms reveal two interesting features that can be tested observationally. The first is that the angle of the polarity inversion line (PIL) changes by a small amount ( $\sim 14^\circ$  difference in figures 6(b)–(d) compared to (a)) as the region grows in size. Emerging twisted tubes show a more substantial rotation of their main polarities (e.g. Hood *et al.* 2009). The second is that the polarities exhibit a tadpole-like structure. This property is similar to twisted models and has been used as an observational indicator for twist in an emerging region (Luoni *et al.* 2011, MacTaggart 2011). Thirdly, there is a developing complex pattern at the PIL. To investigate this property in more detail, we can consider the twist profiles of the region.



**Figure 6.** Synthetic magnetograms of  $B_z$  at the photospheric boundary  $z = 0$  for the B4 field. (a)  $t = 10$ , initial emergence into photosphere, producing a classic bipolar structure. (b)  $t = 30$ , slight rotation of PIL. (c)  $t = 50$ , similar to (b) but with a growing ‘banded’ structure at the centre. (d)  $t = 90$ , little change from (c).

Figure 7 displays maps of the field line twist  $L_f$  at  $z_{\text{ph}}$  for four different times. Figure 7(a) shows the twist profile at  $t = 10$ . The PIL can be seen in white and matches the shape in figure 6(a). At this stage, the majority of the twist is of one sense (negative, blue) except in a thin strip crossing the centre of the PIL (positive, red). As the region evolves, positive twist aligns with the PIL and becomes stronger in magnitude. There remains a complex banded (blue and red) strip that cuts across the centre of the PIL. Away from the PIL, a complex mixed pattern of both positive and negative twist develops. These features convey that the magnetic field remains strongly twisted at the PIL. This is analogous to the twisted tube case, where shear is concentrated at the PIL (Hood *et al.* 2012). The banded structure, however, is generally not seen as an emerging structure in twisted models. That feature and the complex mixing pattern away from the PIL are due to the complexity of the original B4 braid. Figure 8 shows plots of  $L_f$  at the coronal boundary  $z_{\text{cor}}$ . In figure 8(a), the profile is shown at  $t = 30$  and reveals two distinct regions of emergence of relatively weak twist. The boundary between these regions matches the banded structure from figure 7 and can also be seen in figure 4(c). Later, at  $t = 90$ , the twist profile exhibits a complex pattern due, in part, to the undulations caused by dense plasma, cf. figure



**Figure 7.** Distributions of  $L_f$  at the photospheric boundary for the B4 field. (a)  $t = 10$ , the (white) PIL is clear, cf. figure 6(a). (b)  $t = 30$ , there is now a positive twist in the core with a negative outer ring. Additionally there is a banded structure of opposing twist at the centre of the field here. (c)  $t = 50$ , the basic features of (b) are present but there is far more mixing. (d)  $t = 90$ , the mixing pattern has increased with strong twist concentrated at the PIL.

4(d). This pattern, with mixed regions of positive and negative twist on various scales, is similar to twisting patterns found from nonlinear force-free field extrapolations from magnetograms of emerging bipolar regions (e.g. Liu *et al.* 2016). Some coronal field line subsets at  $t = 90$  are shown in figure 9 anchored at various sections of the final coronal  $L_f$  distribution shown in figure 8(b). Figure 9(a) displays field lines traced from a complex mixing region of the  $L_f$  map. These field lines connect across the region and exhibit a complex and twisted geometry. Dipped field lines can be identified and these correspond to the previous discussion on undulations. The field lines that connect across the region also appear to exhibit a sigmoidal geometry. This will be confirmed later when calculating the emission proxy. Figure 9(b) shows field lines that are lower in the corona and have much weaker twist. On either side of the PIL, the plotted arcades are close to potential. This plot shows that even at different heights in the corona, the magnetic field geometry can change drastically.

Figure 10 shows the emission proxy for the emerged B4 field at  $t = 90$ . There are two clear features revealed by this plot. The first is the intense line crossing (0,0) diagonally downwards. This represents the main undulation in the emerging magnetic bubble which,

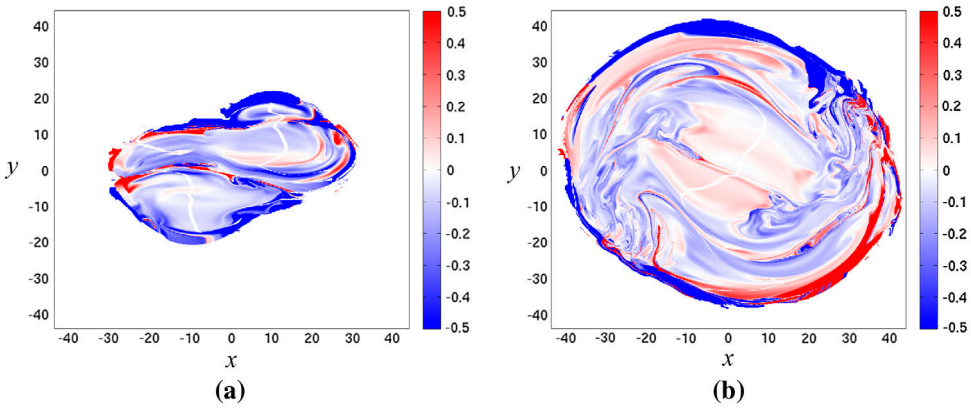


**Figure 8.** Distributions of  $L_f$  at the coronal boundary for the B4 field. (a)  $t = 30$ , the field has emerged relatively recently into the corona and we see some evidence of the complex internal structure of the field with several islands of positive and negative twist. There is a clear inversion line except at the centre of the field where it becomes significantly distorted. (b)  $t = 90$ , the complex mixed structure observed in figure 7 is evident.

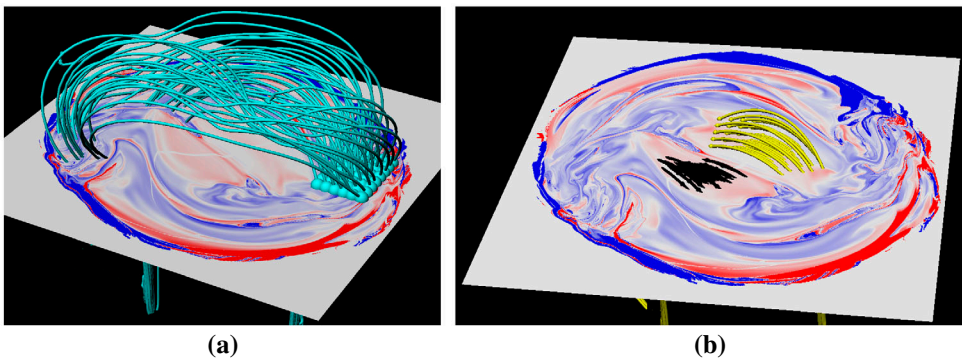


**Figure 9.** Clusters of field lines drawn on regions of the  $z_{\text{cor}} L_f$  plots for the B4 field at  $t = 90$ . (a) displays a set of field lines plotted from the region of mixing on the right hand side of the distribution. The seeds of the field lines are shown as spheres. (b) shows field lines traced in the two distinct regions of weak twist near the centre, the field lines are shown in black and yellow.

as shown in the  $\|j\|$  contours and the  $L_f$  maps, is caused by the emergence of the two-bubble region described above. The second feature is a sigmoid which passes horizontally through  $y = 0$ . Weakly twisted emerging flux tubes also produce weak sigmoids similar to that shown in figure 10. Tubes with stronger twist produce more pronounced sigmoids (Archontis *et al.* 2009). Hence, distinguishing between emergence from a weakly twisted tube and a B4-like braid may prove difficult from studying the emission.

### 3.3. Pigtail field

The pigtail field evolves for  $t \in [0, 100]$ , during which the field expands into the corona, as shown in the current contour plots of figure 11. The general evolution of a rising magnetic bubble with some flux trapped in the photosphere is similar to the B4 case and other twisted models (Hood *et al.* 2012).

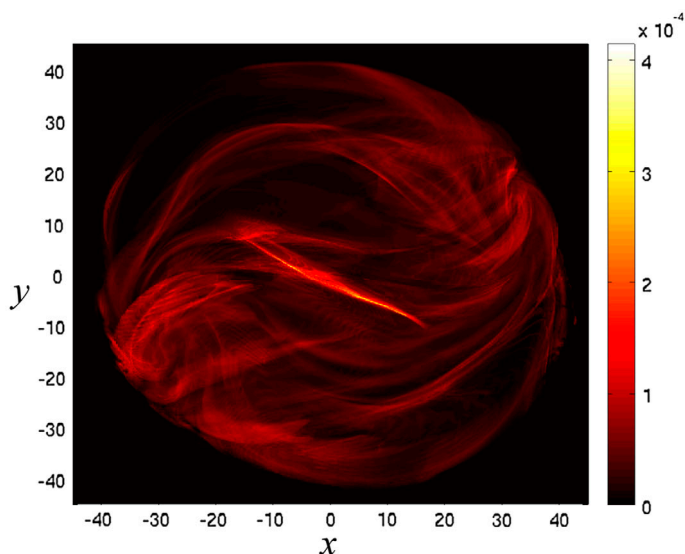


**Figure 10.** Emission proxy for the emerged B4 field in the corona at  $t = 90$ .

As for the B4 case, undulations form, as can clearly be seen in figure 11(d). The morphology differs from the B4 case, however, with the undulations taking a more linear profile. This effect is shown again in figure 12, with plots of  $\|\mathbf{j}\|$  and  $\log \rho$  taken at  $z = 82.5$ . The linear profile of the undulations is suggestive of a weakly twisted magnetic field. This will be confirmed later when examining the twist plots for the pigtail. Figure 13 displays the synthetic magnetograms at  $z_{\text{ph}}$  at four different times during emergence.

The pigtail does not produce the general bipolar structure of the B4 field. Instead, an asymmetric pattern forms, as in figure 13(a), which then develops into a banded structure alternating between positive and negative polarities. Although the internal structure of the B4 field is more complex than the pigtail, the magnetograms of the pigtail emergence are much more complex than those of the B4 field. To see where this banded structure comes from, it is helpful to examine the pigtail field before it emerges. This is displayed in figure 14.

Taking a slice close to the apex of the pigtail field at  $t = 0$ , as displayed in figure 14(a), the resulting synthetic magnetogram is shown in figure 14(b). The pigtail in our model consists of three independent flux tubes. In the magnetogram of 14(b), the image of these flux tubes can be seen as a banded structure. This structure persists to the photosphere and, hence, the photospheric magnetograms reveal the internal structure of the pigtail braid. As mentioned above, the B4 field has a more complex internal structure than the pigtail but a simpler magnetogram. The internal structure of the B4 field consists of flux tubes braided at much finer scales compared to the pigtail. Hence, the B4 field rises to the photosphere as, essentially, one tube. The internal structure of the pigtail, however, consists of three individual flux tubes that remain, to a significant extent, distinct.

Figure 15 displays the distribution of  $L_f$  at  $z_{\text{ph}}$  for four different times. At  $t = 20$ , figure 15(a) shows that the emerging field is initially dominated by positive twist. At later times, this simple picture breaks down into a highly complex pattern. These maps show that although the initial pigtail flux tube has a relatively simple structure, upon emergence

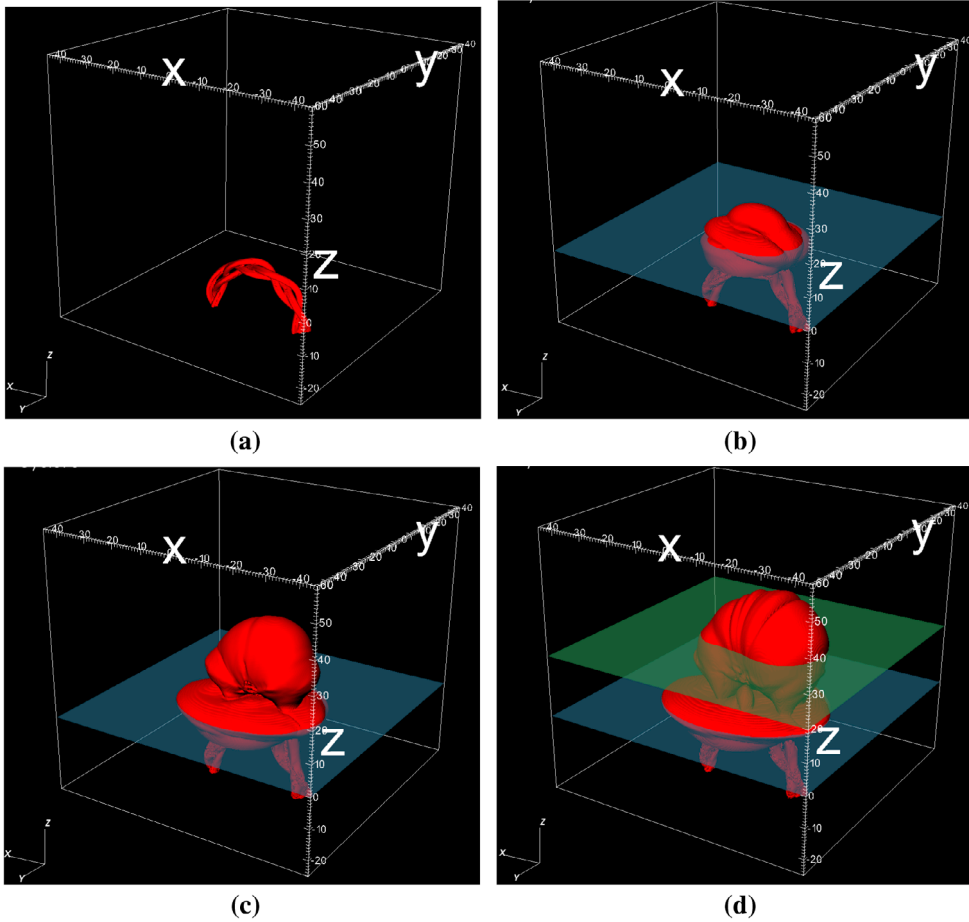
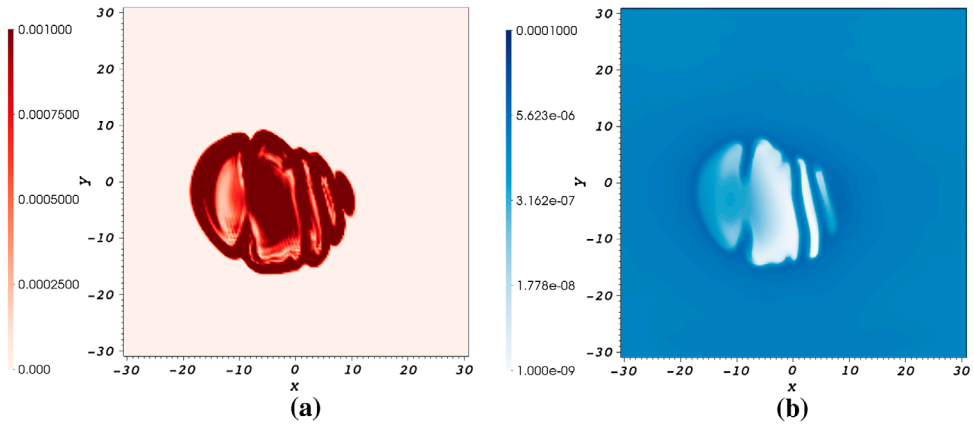


**Figure 11.** Contours of constant current for the pigtail field. (a)  $t = 0$ , the initial pigtail structure. (b)  $t = 30$ , the field has expanded into the photosphere. (c)  $t = 50$ , the field expands significantly. (d)  $t = 100$ , the field has penetrated the coronal region, undulations in the current structure are evident. Grey slice:  $z_{\text{ph}}$ , green slice:  $z_{\text{cor}}$ .

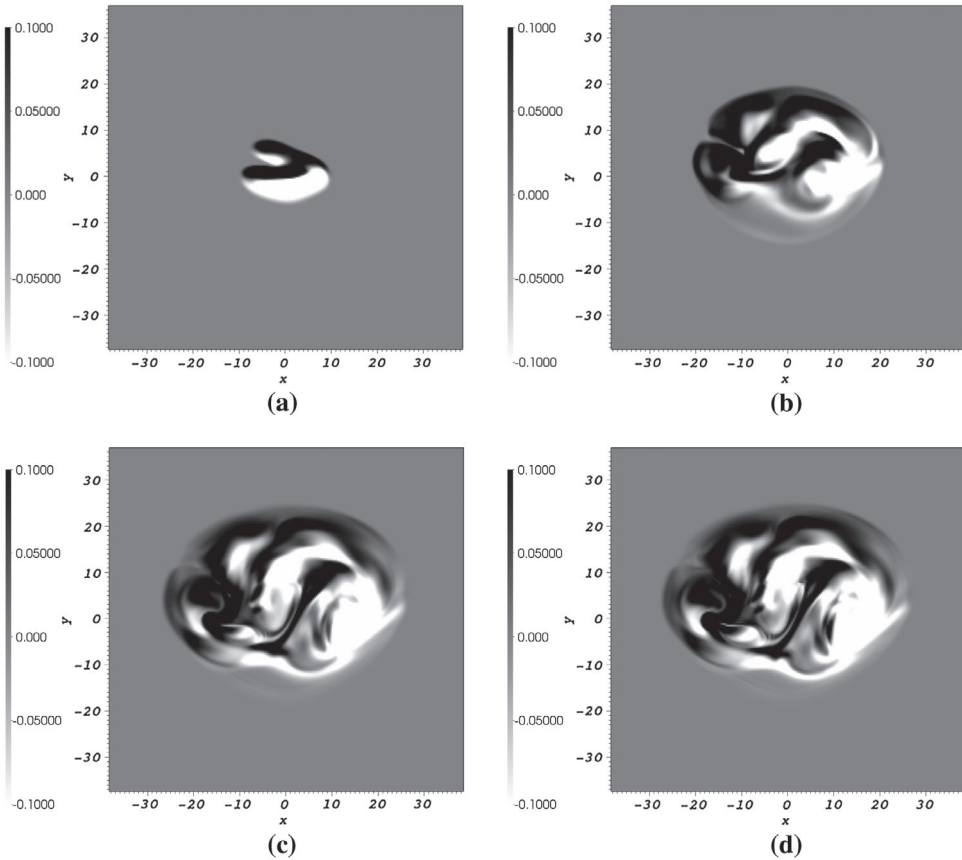
it develops many fine scales in the photosphere. Unlike the B4 map, there is no clearly discernable PIL.

Figure 16 shows the  $L_f$  profiles at  $z_{\text{cor}}$  for four different times. The coronal field is much simpler than that at the photosphere. The PIL is clearly identifiable at all times and is not subject to substantial deformation. The twist is mainly positive and its magnitude within the emerging region is weak. These results are in agreement with the linear morphology of undulations considered earlier, which implied a weakly twisted field. The lack of twist appears to indicate only one of the flux elements composing the initial pigtail has emerged into the corona. This picture, however, is a slight simplification as areas develop in the maps where the twist becomes stronger, e.g. the centre of figure 16(d).

One interesting feature of these maps is appearance of a region of negative twist on the right of the domain, as shown in figures 16(c) and (d). This ‘new’ region is initially of strong negative twist. However, the magnitude of negative twist decays within the new region. Figure 17 shows magnetic field lines plotted within the main emerging region and



**Figure 12.** Slices of the current magnitude and density distributions of the pigtail field at  $z = 82.5$  for  $t = 100$ . (a) the current magnitude (darker colours are higher in magnitude), the ridge structure shown in figure 11(d) is clear. (b) the (logged) density magnitude, the morphology of the distribution matches that of the current distribution in (a).



**Figure 13.** Synthetic magnetograms of  $B_z$  at the photospheric boundary  $z = 0$  for the pigtail field. (a)  $t = 20$ , the initial emergence has two dominant bipoles. (b–d) ( $t = 40, 70, 100$  respectively) the simple bipolar structure is absent and there is a banded structure of positive and negative polarities.

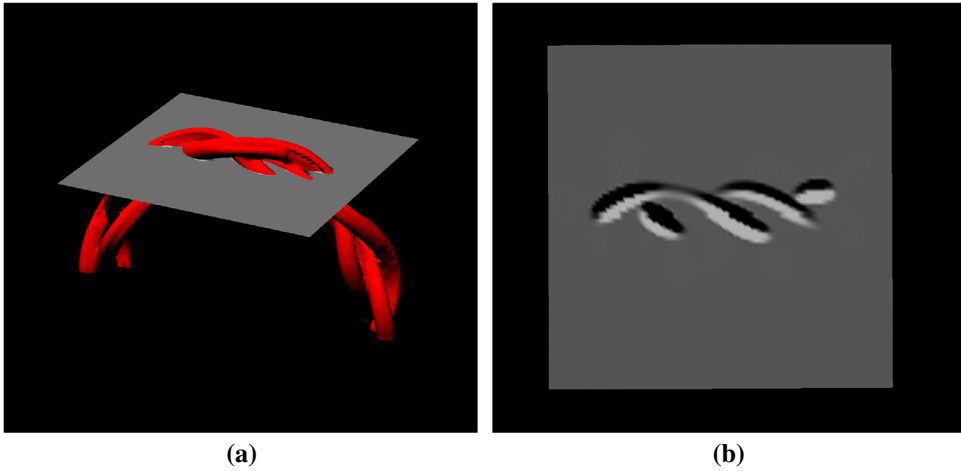


**Figure 14.** An indication of the banded magnetic structure of the pigtail braid at  $t = 0$ . (a) indicates the slice taken near the apex of the braid. (b) shows the magnetogram from the slice in (a).

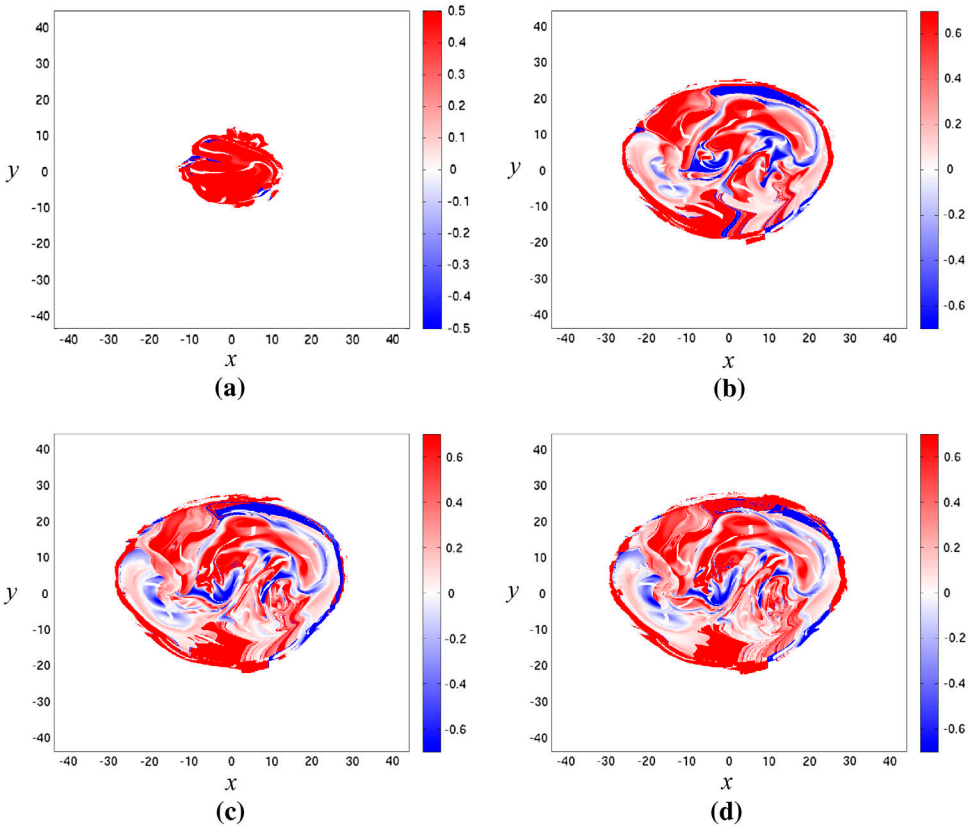


**Figure 15.** Distributions of  $L_f$  at the photospheric boundary for the pigtail field. (a)  $t = 20$ , upon the initial entry into the photosphere the plot is dominated by positive twist. By comparison in (b), (c) and (d) ( $t = 50, 70, 100$  respectively) the picture is far more complex with numerous interspersed islands of both positive and negative twist. There is no coherent inversion line.

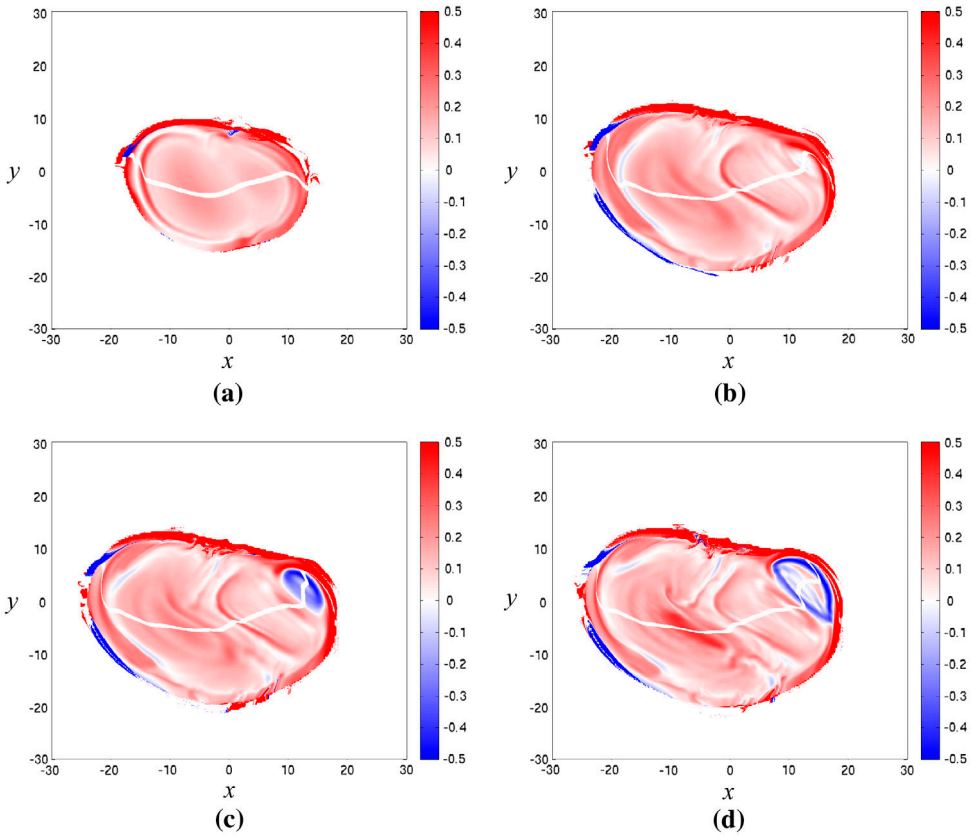
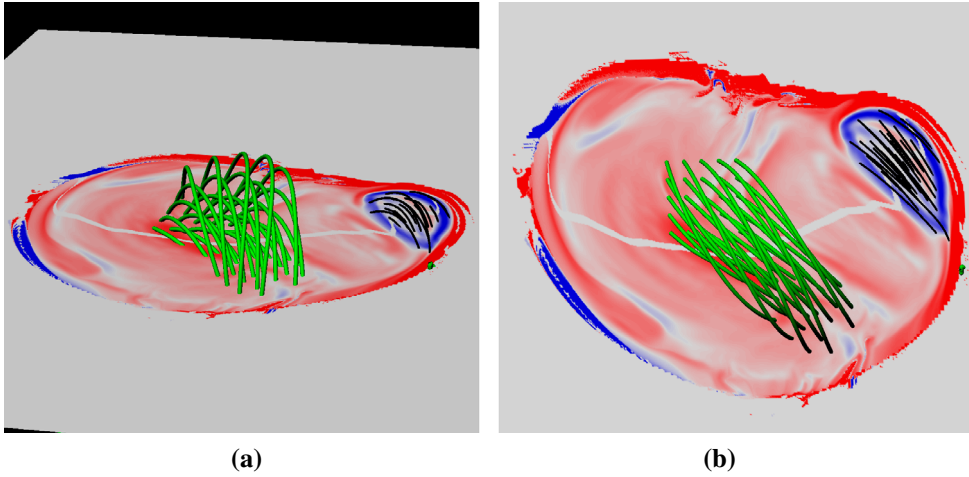


**Figure 16.** Distributions of  $L_f$  at the coronal boundary for the pigtail field. (a)–(b) ( $t = 50, 70$  respectively) the plots are dominated by weak positive values. (c)  $t = 80$ , a small negative region emerges in the upper corner of the distribution, the inversion line remains continuous within this section of the field. (d)  $t = 100$ , the twist of the negative region observed in (c) appears to diminish in magnitude, though some new internal structure forms.

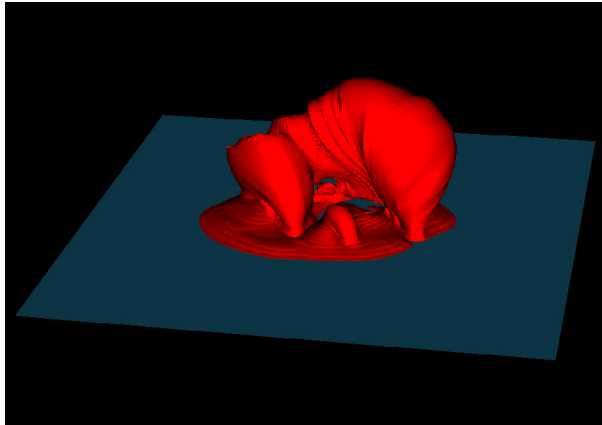
the new region at  $t = 100$ . The  $L_f$  distribution from 16(d) is included to help provide a context. The green field lines are traced over a region of increased positive twist and take the form of a sheared arcade. The black field lines of the new region are, by comparison, much closer to potential. This two-region formation in the corona is due to the staggered emergence of elements of the initial individual pigtail, which, as the magnetograms (figure 13) suggest, remain significantly distinct. When the three tubes that comprise the pigtail reach the photosphere and emerge, one of these tubes forms the main part of the coronal field. The others can also emerge and interact to create the complex twisting pattern in the photosphere. The smaller region in the corona is the result of another of the pigtail tubes emerging.

Figure 18 displays a contour of  $j_x = 0.07$  and highlights that the pigtail field can launch multiple emergence regions. As well as the two regions that reach the corona, indicated in figures 16(c),(d), figure 18 also reveals a third emerging region that has not yet reached the corona.

Figure 19 shows the emission proxy for the emerged pigtail field in the corona at  $t = 100$ . The first observation is that the emission proxy does not exhibit any clear



**Figure 17.** Curves characterising the regions of the coronal  $L_f$  plots at  $t = 100$  for the pigtail braid as seen from the side (a) and above (b). The green curves depict the weakly twisted structure of the bulk of the field which penetrates the corona. The black curves, in the top right of the distribution, depict the structure of the additional emerging island seen in (c) and (d) of figures 16(c) and (d).



**Figure 18.** Contour of  $j_x$  at  $t = 100$  showing the two emerging regions that have reached the corona plus a new emerging region lower in the atmosphere. Grey slice is at  $z_{ph}$ .

sigmoidal structure. This is perhaps not surprising as the total emerging field consists of multiple emerging regions, formed from the tubes of the original pigtail, that are very weakly twisted. The overall shape of the emission proxy is asymmetric, again due to the emergence and interaction of multiple magnetic bubbles. Intense regions highlight the main undulations of the emerging field and the regions of stronger twist.

#### 4. Discussion

In this paper, we have modelled the emergence of braided magnetic fields into the solar atmosphere. Our purpose is to test if the behaviour of such fields, once in the atmosphere, produces dynamics that are consistent with observations. If this is the case, then our results add weight to the theory that small emerging regions can be formed by magnetic flux tubes

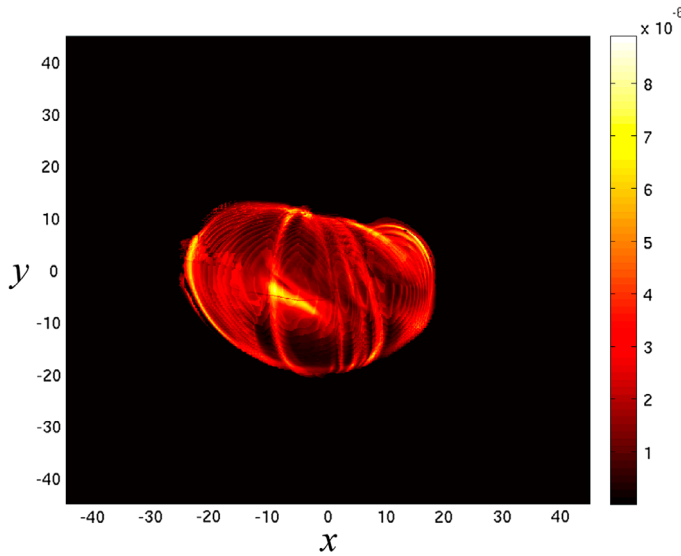


**Figure 19.** Emission proxy for the emerged pigtail field in the corona at  $t = 100$ .

braided in the upper convection zone. We have considered two types of braided field. The first, the B4 field, is the result of a series of staggered twists and has a complex internal structure that varies over length scales shorter than radius of the tube. The second is a pigtail braid that has a simpler (and easily visualized) internal structure which varies on a length scale of the order of the tube radius. Both models have similarities and differences compared to twisted tube models and these have been noted throughout the paper. We shall now highlight some of the observational consequences of our results.

#### 4.1. Magnetograms

The two braid models produce very different magnetograms. Starting with the B4 field, the classic bipolar structure is found. Although this pattern is also found for twisted tube models, there are some differences which are detectable in observations. For the B4 model, the PIL exhibits a small rotation of  $\sim 14^\circ$  during emergence. In twisted tube models, this rotation is much larger and can be  $\sim 90^\circ$ . This small variation of the PIL angle could be an observational indicator that the underlying field is either braided (in a similar way to B4) or is weakly twisted.

Another feature of the B4 magnetograms, that has consequences for observations, is the tadpole structure of the two main polarities. As mentioned previously, this feature has been used as an observational signature of underlying twist in emerging bipolar regions (Luoni *et al.* 2011). The azimuthal component of a twisted magnetic flux tube can produce the tails of the tadpole structure, which would not exist for a potential field. Our results show, however, that a complex braided structure that is not twisted, such as the B4 field, can reproduce the same signature. Hence, other signatures, such as the PIL rotation described above, are required in combination with the tadpole structure in order to better establish whether or not this underlying field is twisted.

The magnetograms of the pigtail field are considerably more complex compared to those of the B4 field. It was described earlier that the banded pattern of the pigtail magnetograms

is due to the internal structure of the emerging flux tube. Unlike the B4 field, which can be thought of as a braid of many fine flux tubes, the pigtail is a braid of three thick tubes. The magnetograms that the pigtail produces have many similarities to regions known as  $\delta$ -spots. The form of  $\delta$ -spot that we are considering here is a complex collection of bipoles emerging together, rather than the collision of two separate active regions (Zirin and Liggett 1987). Almost all models of such regions have been based on emerging twisted flux tubes, either kink unstable (Fan *et al.* 1999, Linton *et al.* 1999, Takasao *et al.* 2015) or exhibiting multiple regions of emergence (Fang and Fan 2015). Our results suggest that  $\delta$ -spots could be due to non-twisted, coarsely braided flux tubes, such as the pigtail. Further work would be required to determine how the atmospheric field in the pigtail model compares with observations of  $\delta$ -spots.

## 4.2. Sigmoids

There is a clear difference between the emission proxies of the two braid models. The B4 field has a sigmoidal shape, suggesting a twisted field. The pigtail field has a structure closer to a potential field with no sigmoidal shape. If an observation produced an image similar to the pigtail emission proxy, then it could be said with confidence that the emerging field is not twisted. For the B4 case, however, this is not so clear as its features are similar to those of twisted tube models. This observational signature, including the others discussed throughout the paper, suggest that it would be difficult to distinguish a B4-type emerging flux tube from a (weakly) twisted tube.

## 4.3. Conclusions

Our results imply the following for the two models considered:

- (1) B4 – the result of braiding many fine flux tubes, leading to a complex internal structure.
  - (a) The field behaves like a weakly twisted tube during emergence.
  - (b) It has observational signatures that correspond to twisted models a tadpole structure in bipolar magnetograms, twist concentration at the PIL and a sigmoidal structure in the atmosphere.
  - (c) The emerging B4 field may be difficult to distinguish, observationally, from an emerging (weakly) twisted tube.
  - (d) Emergence of the B4 field produces local twisting distributions qualitatively similar to those generated from nonlinear force free extrapolations of emerging bipolar regions.
  - (e) The twist maps of the field (figure 9) indicate that the field which enters the corona maintains a significantly complex internal topology. This result is an indication that the complex field topologies found in the coronal region could be injected through the photosphere.
- (2) Pigtail – the result of thick flux tubes braided together.
  - (a) Emergence of the pigtail field produces complex magnetograms reminiscent of multipolar emerging regions ( $\delta$ -spots).
  - (b) Individual tubes of the pigtail emerge to form the coronal field.

- (c) Several parts of the tubes can emerge together and interact in the atmosphere.
- (d) The emerging region is weakly twisted and does not exhibit any obvious sigmoidal structure.

Both models produce dynamics in the atmosphere that can be identified with existing observations and have implications for the interpretation of these observations. The different topologies of the two models are injected into the atmosphere, resulting in different evolutions of the corresponding magnetic fields. Our results show that the emergence of braided fields leads to quantifiable atmospheric dynamics and, hence, adds weight to the theory that small active regions can form from magnetic flux tubes braided in the convection zone.

Our results could have important implications for larger active regions also. The B4 field produces many signatures that are found observationally and are generally attributed to twisted emerging tubes. If the convection zone can braid, in the manner of B4, many small flux tubes into a tube that is larger than the ones considered in this study, it may be the case that active region fields are, therefore, also the result of braided tubes. This would have important implications for the solar dynamo and should be the subject of future work.

## Disclosure statement

No potential conflict of interest was reported by the authors.

## Funding

DM would like to thank the Carnegie Trust for a Research Incentive Grant (Ref: 70323). CP would like to acknowledge the support of an Addison Wheeler fellowship. Computational resources used in this paper are: the EPSRC funded ARCHIE-WeSt High Performance Computer ([www.archie-west.ac.uk](http://www.archie-west.ac.uk)), EPSRC [grant number EP/K000586/1]; the DiRAC 1, UKMHD Consortium machine at the University of St Andrews; the Hamilton supercomputing facility provided by the HPC service of Durham University.

## References

- An, J.M. and Magara, T., Stability and dynamics of a flux rope formed via flux emergence into the solar atmosphere. *Astrophys. J.* **2013**, **773**, 21.
- Antman, S., *Nonlinear Problems of Elasticity*. Vol. 107, Applied mathematical sciences, **2005** (Springer: New York).
- Arber, T.D., Haynes, M. and Leake, J.E., Emergence of a flux tube through a partially ionized solar atmosphere. *Astrophys. J.* **2007**, **666**, 541–546.
- Arber, T.D., Longbottom, A.W., Gerrard, C.L. and Milne, A.M., A staggered grid, lagrangian-eulerian remap code for 3-D MHD simulations. *J. Comput. Phys.* **2001**, **171**, 151–181.
- Archontis, V., Hood, A.W., Savcheva, A., Golub, L. and Deluca, E., On the structure and evolution of complexity in sigmoids: a flux emergence model. *Astrophys. J.* **2009**, **691**, 1276–1291.
- Barker, A.J., Silvers, L.J., Proctor, M.R.E. and Weiss, N.O., Magnetic buoyancy instabilities in the presence of magnetic flux pumping at the base of the solar convection zone. *Mon. Not. R. Astron. Soc.* **2012**, **424**, 115–127.
- Bishop, R.L., There is more than one way to frame a curve. *Am. Math. Mon.* **1975**, 246–251.
- Bushby, P.J. and Archontis, V., Modelling magnetic flux emergence in the solar convection zone. *Astron. Astrophys.* **2012**, **545**, A107.
- Cheung, M.C.M. and Isobe, H., Flux emergence (theory). *Living Rev. Sol. Phys.* **2014**, **11**, 1–128.

- Cheung, M.C. and DeRosa, M.L., A method for data-driven simulations of evolving solar active regions. *Astrophys. J.* **2012**, **757**, 147.
- Emonet, T. and Moreno-Insertis, F., The physics of twisted magnetic tubes rising in a stratified medium: two-dimensional results. *Astrophys. J.* **1998**, **492**, 804–821.
- Fan, Y., Nonlinear growth of the three-dimensional undular instability of a horizontal magnetic layer and the formation of arching flux tubes. *Astrophys. J.* **2001**, **546**, 509–527.
- Fan, Y., The three-dimensional evolution of buoyant magnetic flux tubes in a model solar convective envelope. *Astrophys. J.* **2008**, **676**, 680–697.
- Fan, Y., Zweibel, E.G. and Lantz, S.R., Two-dimensional simulations of buoyantly rising, interacting magnetic flux tubes. *Astrophys. J.* **1998**, **493**, 480–493.
- Fan, Y., Zweibel, E.G., Linton, M.G. and Fisher, G.H., The rise of kink-unstable magnetic flux tubes and the origin of  $\delta$ -configuration sunspots. *Astrophys. J.* **1999**, **521**, 460–477.
- Fang, F. and Fan, Y.,  $\delta$ -sunspot formation in simulation of active-region-scale flux emergence. *Astrophys. J.* **2015**, **806**, 79.
- Hood, A.W., Archontis, V., Galsgaard, K. and Moreno-Insertis, F., The emergence of toroidal flux tubes from beneath the solar photosphere. *Astron. Astrophys.* **2009**, **503**, 999–1011.
- Hood, A.W., Archontis, V. and MacTaggart, D., 3D MHD flux emergence experiments: idealised models and coronal interactions. *Sol. Phys.* **2012**, **278**, 3–31.
- Leake, J.E., Linton, M.G. and Török, T., Simulations of emerging magnetic flux. I. The formation of stable coronal flux ropes. *Astrophys. J.* **2013**, **778**, 99.
- Linton, M.G., Fisher, G.H., Dahlburg, R.B. and Fan, Y., Relationship of the multimode kink instability to  $\delta$ -spot formation. *Astrophys. J.* **1999**, **522**, 1190–1205.
- Liu, R., Kliem, B., Titov, V.S., Chen, J., Wang, Y., Wang, H., Liu, C., Xu, Y. and Wiegelmann, T., Structure, stability, and evolution of magnetic flux ropes from the perspective of magnetic twist. *Astrophys. J.* **2016**, **818**, 148.
- Luoni, M.L., Démoulin, P., Mandrini, C.H. and van Driel-Gesztelyi, L., Twisted flux tube emergence evidenced in longitudinal magnetograms: magnetic tongues. *Sol. Phys.* **2011**, **270**, 45–74.
- MacTaggart, D., Flux emergence within mature solar active regions. *Astron. Astrophys.* **2011**, **531**, A108.
- MacTaggart, D., Guglielmino, S.L., Haynes, A.L., Simitev, R. and Zuccarello, F., The magnetic structure of surges in small-scale emerging flux regions. *Astron. Astrophys.* **2015**, **576**, A4.
- MacTaggart, D. and Haynes, A.L., On magnetic reconnection and flux rope topology in solar flux emergence. *Mon. Not. R. Astron. Soc.* **2014**, **438**, 1500–1506.
- MacTaggart, D. and Hood, A.W., Multiple eruptions from magnetic flux emergence. *Astron. Astrophys.* **2009a**, **508**, 445–449.
- MacTaggart, D. and Hood, A.W., On the emergence of toroidal flux tubes: general dynamics and comparisons with the cylinder model. *Astron. Astrophys.* **2009b**, **507**, 995–1004.
- Magara, T. and Longcope, D.W., Sigmoid structure of an emerging flux tube. *Astrophys. J. Lett.* **2001**, **559**, L55–L59.
- Magara, T. and Longcope, D.W., Injection of magnetic energy and magnetic helicity into the solar atmosphere by an emerging magnetic flux tube. *Astrophys. J.* **2003**, **586**, 630–649.
- Meyer, K.A., Sabol, J., Mackay, D.H. and van Ballegoijen, A.A., The storage and dissipation of magnetic energy in the quiet Sun corona determined from SDO/HMI magnetograms. *Astrophys. J. Lett.* **2013**, **770**, L18.
- Murray, M.J., Hood, A.W., Moreno-Insertis, F., Galsgaard, K. and Archontis, V., 3D simulations identifying the effects of varying the twist and field strength of an emerging flux tube. *Astron. Astrophys.* **2006**, **460**, 909–923.
- Prior, C. and Yeates, A.R., Twisted versus braided magnetic flux ropes in coronal geometry. *I. Construction and relaxation.* *Astron. Astrophys.* **2016a**, **587**, A125.
- Prior, C. and Yeates, A.R., Twisted versus braided magnetic flux ropes in coronal geometry. *II. Comparative behaviour.* *Astron. Astrophys.* **2016b**, **591**, A16.
- Russell, A.J.B., Yeates, A.R., Hornig, G. and Wilmot-Smith, A.L., Evolution of field line helicity during magnetic reconnection. *Phys. Plasmas* **2015**, **22**, 032106.

- Schrijver, C.J., Eruptions from solar ephemeral regions as an extension of the size distribution of coronal mass ejections. *Astrophys. J.* **2010**, **710**, 1480–1485.
- Schrijver, C.J. and Zwaan, C., *Solar and Stellar Magnetic Activity*, Vol. 34, Cambridge astrophysics series, **2000** (Cambridge University Press: New York).
- Stein, R.F., Lagerfjård, A., Nordlund, Å. and Georgobiani, D., Solar flux emergence simulations. *Sol. Phys.* **2011**, **268**, 271–282.
- Stein, R.F. and Nordlund, Å., On the formation of active regions. *Astrophys. J. Lett.* **2012**, **753**, L13.
- Stein, R.F., Solar surface magneto-convection. *Living Rev. Sol. Phys.* **2012**, **9**, 1–51.
- Takasao, S., Fan, Y., Cheung, M.C.M. and Shibata, K., Numerical study on the emergence of kinked flux tube for understanding of possible origin of  $\delta$ -spot regions. *Astrophys. J.* **2015**, **813**, 112.
- Török, T. and Kliem, B., Confined and ejective eruptions of kink-unstable flux ropes. *Astrophys. J. Lett.* **2005**, **630**, L97–L100.
- van Leer, B., Towards the ultimate conservative difference scheme. V – a second-order sequel to Godunov’s method. *J. Comput. Phys.* **1979**, **32**, 101–136.
- Wilkins, M.L., Use of artificial viscosity in multidimensional fluid dynamic calculations. *J. Comput. Phys.* **1980**, **36**, 281–303.
- Wilmot-Smith, A.L., Hornig, G. and Pontin, D.I., Magnetic braiding and parallel electric fields. *Astrophys. J.* **2009**, **696**, 1339–1347.
- Wilmot-Smith, A.L., Pontin, D.I., Yeates, A.R. and Hornig, G., Heating of braided coronal loops. *Astron. Astrophys.* **2011**, **536**, A67.
- Yeates, A.R., Hornig, G. and Wilmot-Smith, A.L., Topological constraints on magnetic relaxation. *Phys. Rev. Lett.* **2010**, **105**, 085002.
- Yeates, A.R., Russell, A.J.B. and Hornig, G., Physical role of topological constraints in localized magnetic relaxation. *Proc. Roy. Soc. Lond. A* **2015**, **471**.
- Zirin, H. and Liggett, M.A., Delta spots and great flares. *Sol. Phys.* **1987**, **113**, 267–281.